Terahertz time-domain spectro-imaging and hyperspectral imagery to investigate a historical Longwy glazed ceramic

Frédéric Fauquet, Francesca Galluzzi, Philip F Taday, Rémy Chapoulie, Aurélie Mounier, Ayed Ben Amara, Patrick Mounaix

scientific reports

Check for updates

OPEN

Terahertz time-domain spectro-imaging and hyperspectral imagery to investigate a historical Longwy glazed ceramic

F. Fauquet[1], F. Galluzzi[3], Philip F. Taday[2], R. Chapoulie[3], A. Mounier[3], A. Ben Amara[3] & P. Mounaix[1]✉

In this paper, we present the potential of Terahertz Time-Domain Imaging (THz-TDI) as a tool to perform non-invasive 3D analysis of an ancient enamel plate manufactured by Longwy Company in France. The THz data collected in the reflection mode were processed using noise filtering procedures and an advanced imaging approach. The results validate the capability to identify glaze layers and the thickness of ceramic materials. To characterize the nature of the pigments, we also use with X-ray images, visible near-infrared hyperspectral imaging spectroscopy, and p-XRF (portable X-ray fluorescence) to qualitatively and quantitively identify the materials used. The obtained information enables a better understanding of the decoration chromogens nature and, thus, to determine the color palette of the artists who produced such decorative object. We also establish the efficiency of a focus, Z-tracker, which enables to perform THz imaging on non-flat samples and to attenuate artifacts obtained with a short focus lens. Then, 3D images are extracted and generated, providing a real vision. We also report the evaluation of the internal damage state through the detection of fractures.

Keywords Earthenware, Polychrome glazes, Pigment, Ceramics, p-XRF, Hyperspectral imaging, Infrared false color, Terahertz imaging, Thickness, Fracture, Non-destructive analyses

The conservation of cultural heritage greatly benefits from innovative scientific techniques, which have an important impact. Given the value and exclusivity of art pieces, non-invasive diagnostic methods are highly esteemed by conservators[1]. Terahertz (THz) waves have shown their capabilities to provide structural information about materials, as well as data about their chemical nature in art science[2,3]. While the ultraviolet penetration length is limited to varnish layers, visible light to paint layers, and infrared to *imprimitura* layers, THz waves can reach the preparation layers and substrate. Terahertz time-domain imaging (THz-TDI) is used to analyze paintings[4–6] because of its penetration depth. Reconstructing three-dimensional air gaps or material structures within those objects was also demonstrated, which could be an invaluable tool for the evaluation of damage[7] and restoration of paintings, pottery, sculptures, buildings, etc. Moreover, measuring the varnish layer is possible and permits the curator to restore such a layer without altering the paint layer underneath[8]. Similarly, assessing the physical characteristics of the stratigraphy, not only across a painting but also in-depth, is one of the most important procedures for gaining insight into its structure[9]. Using THz pulsed time-domain imaging, the internal structure of a painting can be observed layer by layer by detecting the reflection-pulses generated at the interfaces as the THz pulse transmits, and a cross-sectional image can be reconstructed from the output data[10,11]. Terahertz is rarely used as a diagnostic tool for ceramic fabrics but it can provide information about their layered structure and spatial dielectric properties[3,12–15]. Moreover, information regarding internal features is crucial for determining the state of conservation of a glazed object, highlighting detachments, inhomogeneities, or other defects under the surface. Pottery is one of the oldest human inventions that originated before the Neolithic Period. The earliest known pottery vessels were discovered in Jiangxi, China, dating back to 18,000 BC. The pottery techniques evolved with knowledge and spread all over the world[16], among which French porcelain is famous worldwide thanks to an emblematic city: Limoges. French porcelain is a permanent tableware, characterized by refinement,

[1]Laboratoire IMS-UMR 5218 CNRS, Université Bordeaux, Bat A31, 351 cours de la libération, 33405 Talence, France. [2]TeraView Ltd., 1, Enterprise, Cambridge Research Park, Cambridge CB25 9PD, UK. [3]Archéosciences–Bordeaux: Matériaux, Temps, Images et Sociétés-UMR 6034, Domaine Universitaire, 33607 Pessac Cedex, France. ✉email: patrick.mounaix@u-bordeaux.fr

historical know-how, and extraordinary originality. Ceramic can be classified into three categories: porcelain, earthenware, and stoneware. The main differences between them are the composition, firing technique, and temperature. This firing process produces vitrification, which provides strength, transparency, and a non-porous nature to the porcelain[3,12]. In this paper, we analyze an ancient enamel plate made by the "Longwy Company" to report on the 3D structures of the plate, the potential of separating the diverse coloring techniques, and evaluating the thickness of this ceramic material. The paper is organized as follows: the investigated sample is described in section "Enamel technique"; section "Method" explains THz data acquisition and processing analysis of time-domain data, and the results of measurements made on an ancient enamel plate are presented; section "Results" summarizes the results with imaging and reports on the detection of fractures in ceramics, while the characterization of pigments through hyperspectral visible near-infrared imaging spectroscopy and p-XRF are discussed in section "Discussion"; "Conclusions" and future works are provided. The "Annex" includes the methods and comprehensive results from spectroscopic and elemental analyses. The acquired information made it possible to better apprehend the nature of the decoration chromogens and, thus, to establish the color palette of the industry that produced this type of decorative object. We also demonstrate the efficiency of a focus, Z-tracker and express the possibility of performing THz imaging on non-flat samples. Then, 3D images are extracted and generated, providing a real vision of the 3D object.

Enamel technique

Born in the Lorraine region of France, the foundation of ceramic arts, the "Manufacture des Emaux de Longwy" 1798, was the first ceramic industry in France created in the eighteenth century. The enamel manufacturing process involves numerous expert artisans who know how to create it. To create a single piece, at least seven different techniques are required: modeling, casting, finishing, pressing, cooking, and cracking. This process can take up to 100 h. The transformation of crystal powder into enamel with magical luminosity is a precise task requiring a high level of skill and expertise. For more than a century, Longwy has been producing enamels in earthenware. The production of ceramic pieces decorated with relief polychrome glazes consists in printing the ornamentation in black on the raw biscuit, then filling each cell, thus surrounded drop by drop with colored enamel.

To make ceramic objects by casting, we do not start from clay bread, but from clay in liquid form. They used dehydrated clay to liquefy water. This liquid clay was then poured into plaster molds to obtain a given shape. The modeling workshop created a plaster model, which was then used to create a hollow plaster mold for pouring slip, a mixture of kaolin, clay, and water. The plaster mold absorbs liquid from the slip, forming a crust along its walls once it reaches a thickness of 7/8 mm. The excess slip was emptied after the mold was turned over, and the piece was left to dry in the mold before being removed and air-dried. For plates, ancient and well-known techniques consist of shaping one's clay with the help of a machine called a Potter's wheel. Recently, modern techniques have used molds. Then, the piece was fired at 1050 °C overnight.

The resulting white clay is called biscuit. The biscuit is printed with a line of black ink that repeats the decoration of the piece and partitions the colors, thereby preventing them from mixing. Since the nineteenth century, the printing process has been extensively developed to reduce costs. The procedure starts with a patterned metal printing plate similar to those used for engravings or etchings on paper. The plate is used to print the pattern on tissue paper, using mixes of special pigments that stand up to firing as the "ink." The transfer is then placed pigment-side down onto the piece of pottery so that the sticky ink is transferred to the ceramic surface. Before transfer printing, ceramics were hand-painted, which is a laborious and costly process. Each cell created by the line was then filled with colored enamel using a drop-by-drop technique[17]. As the drop of enamel dries almost instantly on contact with the biscuit, it is impossible to "paint" this piece, hence the use of the technique which consists of placing one drop of enamel next to another until the color cell is completely filled. Each alveolus created by the line was then filled with colored enamel using the drip technique. After the object was completely enameled, it was fired at approximately 750 °C overnight. The piece is then retouched with overlay, requiring a second firing at 750 °C; then, gold is deposited onto the decoration, and the piece is fired again at 600 °C.

Figure 1 presents a central picture of plate with a colored "phoenix" in the center. The layer of colored enamel is unusually thick and produces a volume and depth of color that is generally impossible to reproduce in decorated ceramics. The external diameter was 45 cm. As the designation suggests, relief glazes take their name from the line that outlines the pattern and hold the colored glazes deposited in the various areas thus formed. The last painter applied the colors (pigments with frit) in light touches on the enamels in relief to provide illumination to enrich the décor, such as the pink color on the trees, the ramifications on the leaves, and all the details inside the phoenix bird.

Method

Let's remind you that THz radiation lies between infrared and microwaves of the electromagnetic spectrum, and has a frequency range between 0.1 and 10 THz (or wavelengths between 3 mm and 30 μm). THz radiation is non-ionizing and due to its nature penetrates most dielectric materials. It has dipole selection rules which interacts with both the intramolecular and intermolecular motions of solid matter[18,19]. One of the interesting features of THz radiation is that it can propagate several mms into a sample which allows for the characterization of materials that are quasi-transparent to X-rays. This paper for first time complementary information provided by IR multispectral imaging, X-ray (Fein Focus nano focus, 10–160 keV), and terahertz tomography[20]. THz pulses are produced by focusing ultrafast (120 fs) pulses of near-infrared light (780 nm) onto the gap between the electrodes deposited on LTG-GaAs (TeraPulse, Lx, TeraView, Cambridge UK). A signal-to-noise ratio (SNR) of approximately 80–90 dB was achieved. THz-TD imaging is based on the emission of a picosecond short pulse, that is a THz electromagnetic pulse, which is reflected in the sample under test and interacts with it. Reflected pulses formed by the sample surface and each further inner interface appearing between materials with dissimilar

Figure 1. Picture of the plate (**a**) center and (**b**) global view of the sample (diameter of the plate: 45 cm).

refraction indices are collected and studied as a function of the time-of-flight (ToF), that is, the total propagation time from the emitter to the material interface and returning back to the receiver. The first reflection is due to the interface between air and the outer surface of the sample, and subsequent pulses correspond to internal material interfaces, giving rise to a complex mixed-signal[21]. Therefore, the THz waveform composed of a single point contains the depth profile of the sample at that point, while a bi-dimensional cross-sectional image (also called B-scan) is obtained by collecting data along a trajectory. Finally, the raster scan of an area generates a data cube from which different pictures of the sample can be extracted by displaying different values obtained in the time or frequency domains.

To obtain the best possible lateral resolution, a short focal length must be used to focus the THz beam onto a target or sample, resulting in a depth-of-field that is a few times the wavelength. Ideally, when imaging a planar object, we want to keep the target surface within a few hundred micrometers of the focal plane. The standard Lx PolyScan gantry unit features manual depth adjustment to set the proximity of the sensor relative to the target surface (the focus). The Lx PolyScan Head classically consists of a terahertz emitter and receiver placed adjacent to each other and focused with either a 7-mm or 18.5-mm focal length lens. In our experiment, these lenses were made of high-resistivity silicon. For samples with irregular surfaces, we added and compared a third motion axis to the Lx PolyScan unit to permit automatic adjustment of the focal plane with respect to the sample. The details of the performance are given in "Annex". To perform this measurement, we mounted a laser-range gauge at a 30-degree angle near the terahertz focusing optics. To keep the terahertz focus at the object surface, the instrument control system performs a raster scan with a laser range gauge of 10–20 scans before the terahertz focal spot. This software developed a topological map of the surface to be scanned. The position of the terahertz optics is continuously updated using a topological map. This keeps the terahertz beam focused on the surface of the object. The software allows the user to either keep the focus on the surface of the object or to offset the focus by up to 3 mm to examine the subsurface structure.

Results

To evaluate the refractive index from a raw frequency image, a reference electric field must be measured. $E_r(\omega)$ refers to the electric field generated by the acquisition system. The reference, $E_r(\omega)$, is obtained by placing a metal plate that is precisely located where the surface sample was positioned for object imaging. From the reference electric field $E_r(\omega)$, the experimental reflection transfer function $T_s(\omega) = E_s(\omega)/E_r(\omega)$, can be calculated, $E_s(\omega)$ is the sample frequency-dependent electric field. The experimental reflection transfer function $T_s(\omega) = E_s(\omega)/E_{ref}(\omega)$, can be calculated, $E_s(\omega)$ is the sample frequency-dependent electric field. The transfer function T_s (ω) is a function of the refractive index $n(\omega)$ and extinction coefficient $\kappa(\omega)$ of the sample under inspection[22]. $E_s(\omega)$ depends on Fresnel's coefficients for transmission $T_s(\omega)$ and reflection $R_s(\omega)$. The complex refractive index $n^*(\omega)$ at each pixel location can be extracted from the experimental transfer function Ts (ω) by solving an inverse electromagnetic problem[23]. This function denotes the disagreement between the experimental waveform $E_s(\omega)$ and waveforms[24]. We performed the extraction on a flat area of the blue substrate near the main fracture. An average value of around 2.5 ± 0.1 like a standard glass, is found, and the local thickness is very large for an enamel layer around 650 µm (confirmed by an optical thickness gauge near the fracture).

We show THz images based on raw THz signals obtained directly from the scan. The motorized stage allows the scanning of a surface of 200×200 square millimeters which is less than the total surface area of the plate.

THz C-scans (two-dimensional appearance of the data displayed as a top planar view of the decoration) are shown in Fig. 2.

For the THz C-scan in the time domain shown in Fig. 2a, the selected imaging contrast mechanism was the peak-to-peak amplitude of the reflected THz signal (i.e., the peak-to-peak amplitude of the main temporal signal). The THz C-scan in the frequency domain can also be displayed by taking the Fourier transform of the temporal waveform at each pixel and showing the magnitude of the frequency components in a given frequency window or at a specific frequency. THz C-scans mainly present the THz response of the surface material, and they reveal the surface roughness or orientation with respect to the generated THz beam, as well as evidence of subsurface features. In Fig. 2a, the Fresnel coefficient between the first ceramic layer and air depends on the refractive indices of the material; however, in our case, the image of the plate is mainly correlated to the flatness of the sample. A clear intensity gradient was observed from the center to the exterior, which was associated with the 3D surface morphology of the plate. In the presence of surface irregularity, reflection of THz radiation occurs, and consequently, there is a weaker specular signal leading to a gradual decrease in the intensity. Nevertheless, some identified zones present different reflectivity, such as the pink painting overlaying small trees and some dark green on leaves. A video permits the superposition of THz and visible images. Figure 2b, which is an intensity X-ray image, reveals identical features at the same location, while Fig. 2c serves as a guide for the localization of the different color areas of the plate. Because the pigment-colored enamel used a drop-by-drop technique, it presented a slightly concave shape due to the molten procedure, the THz beam was partially reflected out of the sensor, and the outline of each enamel zone was detected to be larger than the real zone. This irregular surface shape was also observed in the B-scan.

However, a THz C-scan is an X, Y image of an object, and a THz B-scan (two-dimensional presentation displayed as a cross-sectional view of the sample) provides depth information along a line in the X and Y planes[14,25]. The optical delay can be converted into depth information by determining the refractive indices of the various layer materials. The THz B-scans based on the raw data with the two cross-sections are plotted in Fig. 3a, their positions are displayed in Fig. 3b. The different lines are due to the magnitude of the reflected signal at a given optical delay, and each linked identical interface encountered by the propagating beam. The first large feature of the optical delay is the reflection of the first ceramic layer. The complexity of the layered structure can be clearly observed, corresponding to the time delays from 0 to 10 ps after the main peak. A pronounced horizontal concavity was observed because the sample was evidently not flat while the detector was scanning in a constant vertical position. Based on these results, we can consider that only a 50 mm circular zone maintains the main reflected peak in the Rayleigh range, and the data are reliable and easy to analyze. The rest of the data provides the relative position of the interface with the sensor, but the amplitude information is incorrect because of reflection losses. To complete the 3D rendering of the plate and compensate for this drawback, we completed the acquisition with a Z-tracker. Details of the procedure are provided in "Annex". To obtain the best possible lateral resolution, a short focal length must be used to focus the THz radiation on the target or sample. This results in a depth-of-field of few wavelengths. Ideally, when imaging a planar object, we want to keep the target surface within a few hundred micrometers of the focal plane. With a nonplanar surface, it is impossible to maintain the surface at the focal plane over a large imaging area. Figure 3c displays a B-scan measured using the Z-tracker option. The time peak position was kept almost constant within 1 ps over the entire scan area.

Consequently, we can merge both the information and the 3D rendering the real shape of the plate. Figure 4a displays the ceramic object and expresses the concavity in the X- and Y-directions. The height difference from the center to the edge is approximately one centimeter which is the order of magnitude observed on the plate. In Fig. 4b, we slightly rotated the data to provide evidence of a "flat zone" in the center of the ceramic. Figure 4c presents the 3D reconstruction of the central area of the plate.

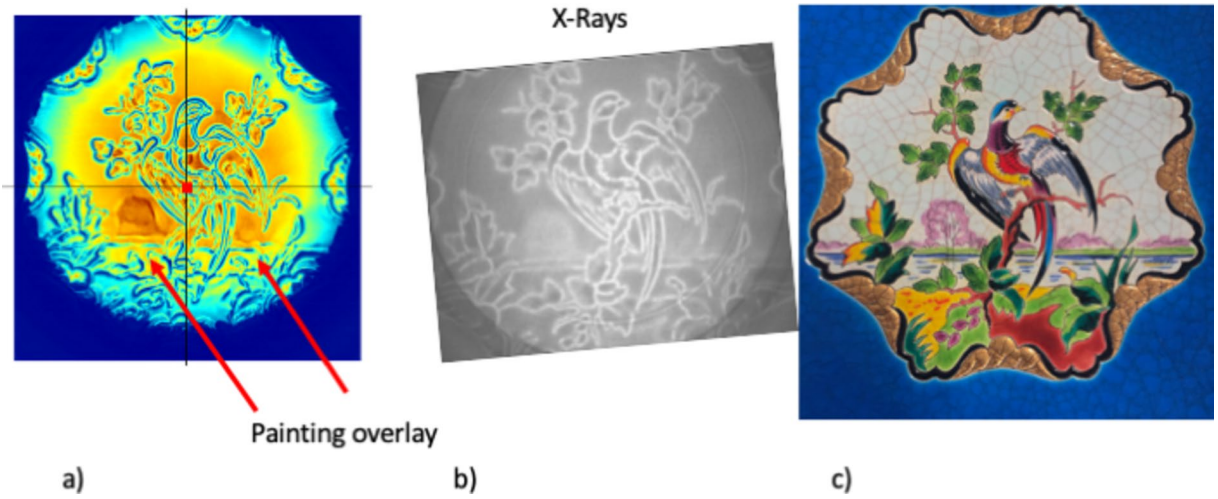

Figure 2. (**a**) Peak-to-peak raw data of the central area of the plate terahertz map, (**b**) X-ray intensity, (**c**) visible picture of the Phoenix.

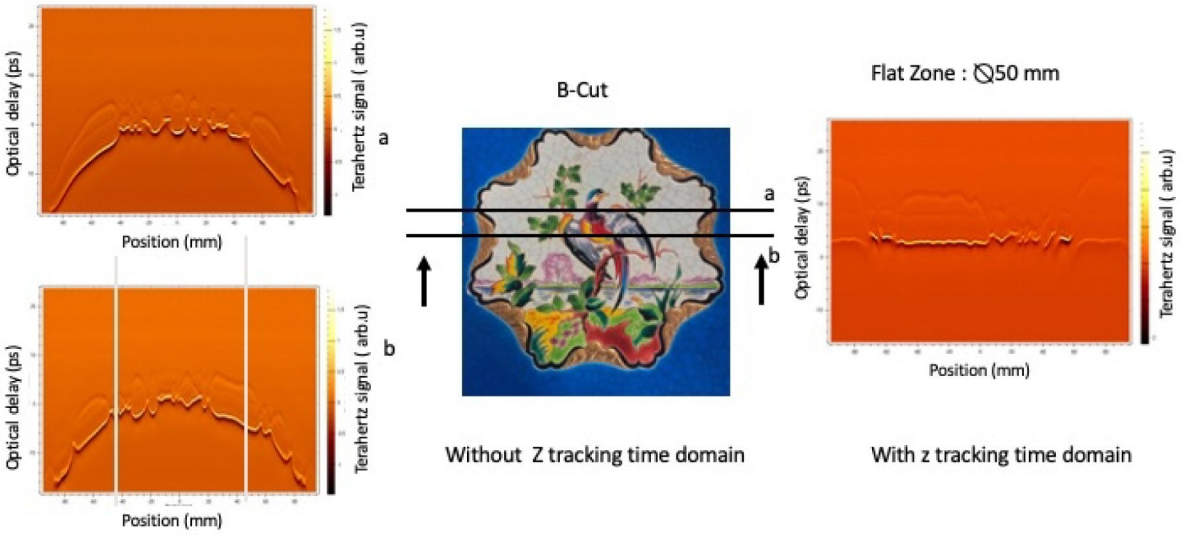

a) b) c)

Figure 3. Different terahertz B-scan presented at position A and B without Z Tracker (**a**) and with Z-Tracker (**c**).

A meshed network of tiny fractures or hairline fissures in the enamel is referred to as "crazing" or "fissuring," and it can result in the total loss of a clean appearance for food or drink. The only reason is that with time, different tensions develop between the biscuit and the glaze underneath. The item was not designed to endure the heat stress caused by pouring boiling drinks or rinsing at temperatures higher than 80 °C. The body has less physical mass because it is more porous than the glaze covering it. Different expansions occurred owing to the slower rate of heating compared to the glazing layer. Masses exhibit distinct contractions under cold conditions and expansions under hot conditions. Consequently, the link between these two materials fractures and creates cracks.

These tiny fissures become larger with use and eventually create surfaces and ridges that allow foreign materials to build. For example, tea and coffee leave unsightly coloring in fractured glazes. In general, the likelihood of cracking increases with a decrease in the firing temperature. Given that only ceramics may develop these types of glaze cracks, this further suggests that there is no flaw in porcelain. Hard porcelain has a physical density similar to the glaze's since it is fired at a minimum temperature of 1350 °C. As so, there is zero chance that it will crack. Figure 5a presents the THz C-scan in the time domain shown equivalent to Fig. 2a, the peak-to-peak amplitude of the reflected THz signal is extracted and displayed using the z-tracker scan. The intensity is clearly homogenous without artifacts and now the large crack with a lambda shape (λ) is now visible between the central-colored zone and a golden decoration. An X-ray image presented in Fig. 5b validates the first observation and also small fractures are detected and they are diverging from the main failure along three directions. With our apparatus, X-ray imaging fails to reveal hairline cracks in ceramics due to several factors: The two main reasons are first resolution limitations: Standard X-ray imaging has limited spatial resolution, meaning it might not be able to detect very fine details like hairline cracks, which are extremely narrow and small. The second origin is a contrast issues: Hairline cracks may not create sufficient contrast in X-ray images. X-rays work by detecting differences in material density and thickness. Hairline cracks are often too narrow to cause a significant difference in X-ray absorption, making them hard to distinguish from the surrounding material.

Figure 6 presents a focus on the main λ fracture. A raster scan is performed with a spatial step of 100 µm. The main fracture is perfectly resolved and surprisingly, the hairy fracture network is resolved and clearly detected. We also present the 3D reconstruction of the fracture. Figure 7b is a B-scan with the temporal reflected signal obtained for position 1 near the fracture and position 2 inside the fracture (red square) reported on the C-scan Fig. 7a. The reflected signal 1 is displaying three main peaks, the first air-enamel, the interface between the biscuit and the enamel and the last interface plate-air. This is corroborated by signal 2 where the second peak is enhanced due to the changing Fresnel reflection coefficient between air and the biscuit. The depth resolution of THz reflectometry is sufficient to resolve the two-layer stratigraphy of the ceramics.

Discussion

In our study, we employed three complementary analytical techniques—THz-TDS, p-XRF, and Vis–NIR HIS to achieve a comprehensive understanding of the Longwy plate.

Time-domain terahertz-transmission-line-detector (THz-TDS) measurements offer insights into the temporal delays and amplitude fluctuations of terahertz (THz) pulses traversing or reflected by a given material. These measurements can be employed to assess the material's intrinsic properties, including its conductivity and refractive index. They also enable the detection of defects and inclusions within the material. However, it should be noted that THz-TDS measurements are not sufficient to provide a comprehensive understanding of the object under study. p-XRF provides elemental composition, which complements the molecular and structural

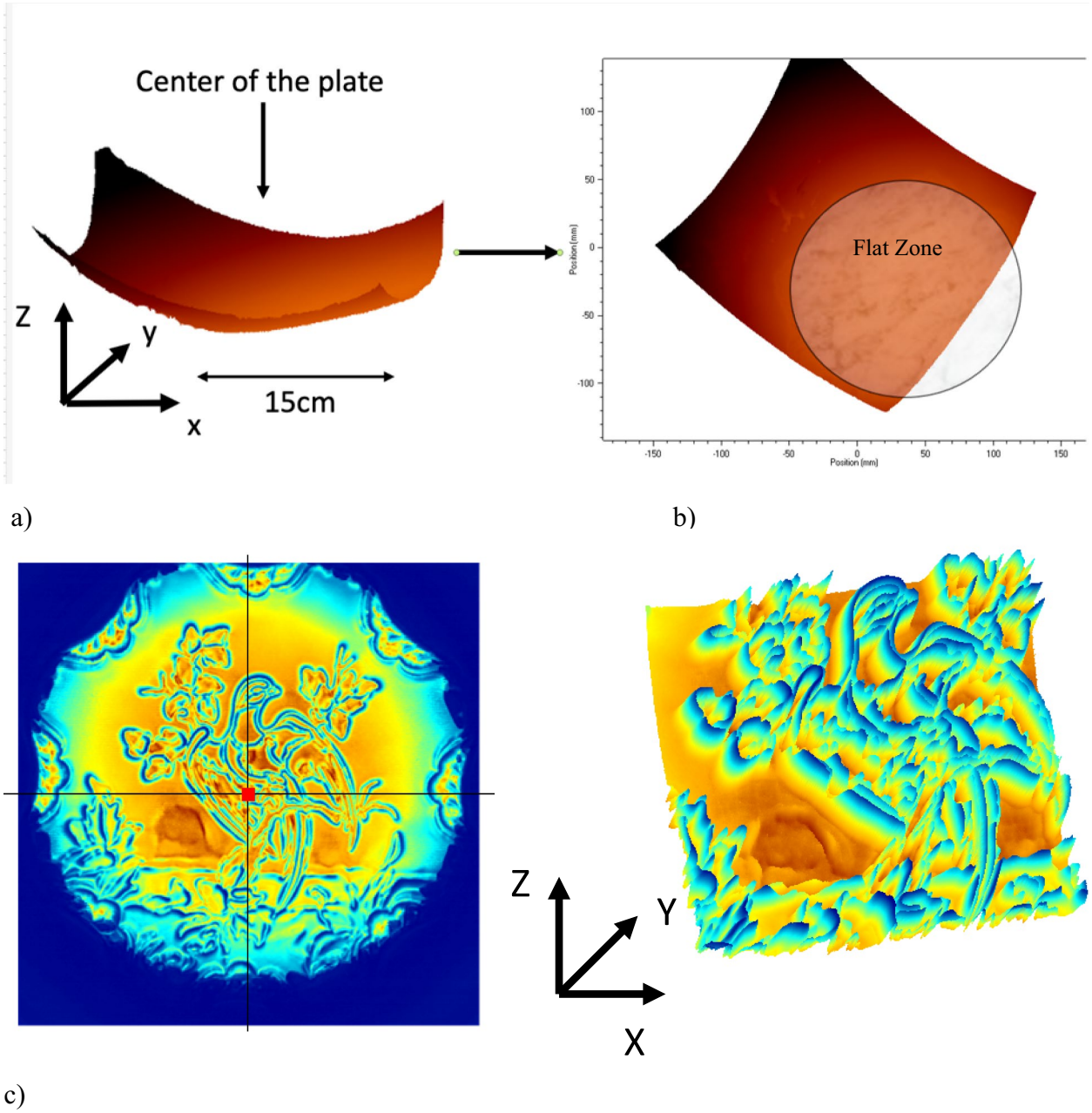

Figure 4. Biconvex real shape of the plate extracted from t-o-f and Z tracker acquisition, 3D representation of the plate shape, (**b**) delimitation of the flat area in the center, and a large crack is barely observed. (**c**) 3D representation of the phoenix in the center of the plate; the difference depth is 0.4 mm.

information obtained from THz-TDS. The spectral data from Vis–NIR HSI can be used to validate the spatial distribution and specific identification of pigments. By combining the elemental and spectral data from p-XRF and Vis–NIR HSI with the structural and defect analysis from THz-TDS, we achieve a more comprehensive understanding of the pigments and their application methods[26]. This integrated approach allows us to better interpret the historical and technical aspects of the ceramic production processes.

Then, we perform two non-invasive analytical techniques, portable X-ray fluorescence (p-XRF) and visible near-infrared hyperspectral imaging spectroscopy (Vis–NIR HSI), to characterize the glaze and the coloring agents in the decorative ceramic plate from the manufacturing company Longwy. Details of the techniques employed and the main results are presented in the "Annex", while the obtained results are resumed in Table 1. Infrared false colors (IRFC) images facilitated the distinction of chromogen agents of similar color but different compositions (such as copper-based and cobalt-based blue regions that appeared dark blue and red, respectively).

The data showed a great variety of chromophores and pigments used to achieve a wide range of hues. That showcased a noteworthy palette and color proficiency within the manufacturing industry. The procedure and results for blue and green colors are detailed hereinafter as examples.

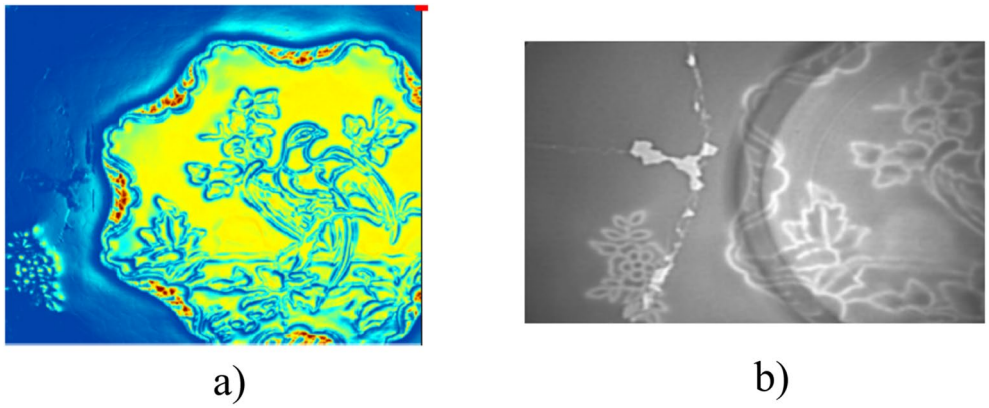

Figure 5. (**a**) Peak to Peak THz image with tracking. (**b**) X-ray image of the fracture.

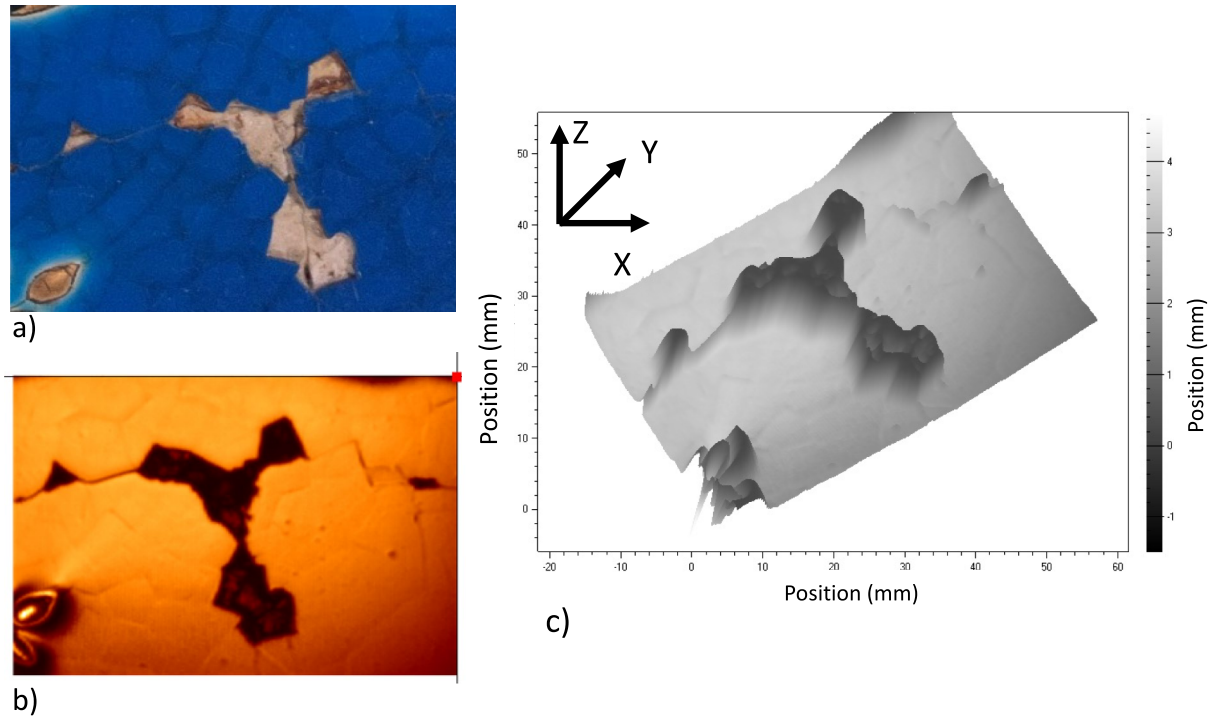

Figure 6. Detail of the "λ" plate fracture showing the base ceramic material with fissures (**a**) visible image, (**b**) THz image, (**c**) 3D representation of the fracture.

Through hyperspectral spectroscopy analysis combined with Spectral Angle Mapper (SAM) classification for data cube processing, it was determined that the pigment responsible for the bright blue hue surrounding the central scene was also implemented in a portion of the bird's tail and head (Fig. 8a). The assumption is further confirmed by the IRFC image, which displays consistent dark hues in these areas, also dismissing the possibility of the use of cobalt-based pigment, typically identifiable by its red coloration in such imagery[17] (Fig. 8b). In Fig. 8c, the reflectance spectrum of these regions (endmember 1) showed a broad absorbance from 700 to 900 nm, aiding in identifying the chromophore as Cu^{2+} in a $3d^9$ state with octahedral coordination ($^2E_g \rightarrow {}^2T_{2g}$)[27]. The detection of copper was confirmed by elemental analysis (p-XRF), which also revealed the presence of iron. The lack of spectroscopic identification of the element can also be explained by the impossibility of detecting the characteristic absorbance of Fe^{3+} ions in tetrahedral coordination ($^6A_1 \rightarrow {}^4T_1(D)$) at 380 nm attributed to the range limits of the implemented camera[28]. The turquoise-green hues observed in both the sky of the bird scene (endmember 2) and the back of the plate share a common composition, relying on copper and iron chromophores. This conclusion has been drawn from the characteristic broad absorbance peaks of Cu^{2+} around 800 nm and one slight peak of Fe^{3+} at 440 nm ($^6A_1 \rightarrow {}^4A_1(G)$[28]. The broader reflectance peak of the spectrum, spanning from 462 to 563 nm, might be highlight that the light blue tone was achieved by incorporating a reduced amount of copper compared to the deeper blue hue of endmember 1. The detection of both copper and iron with p-XRF strengthened their assumption.

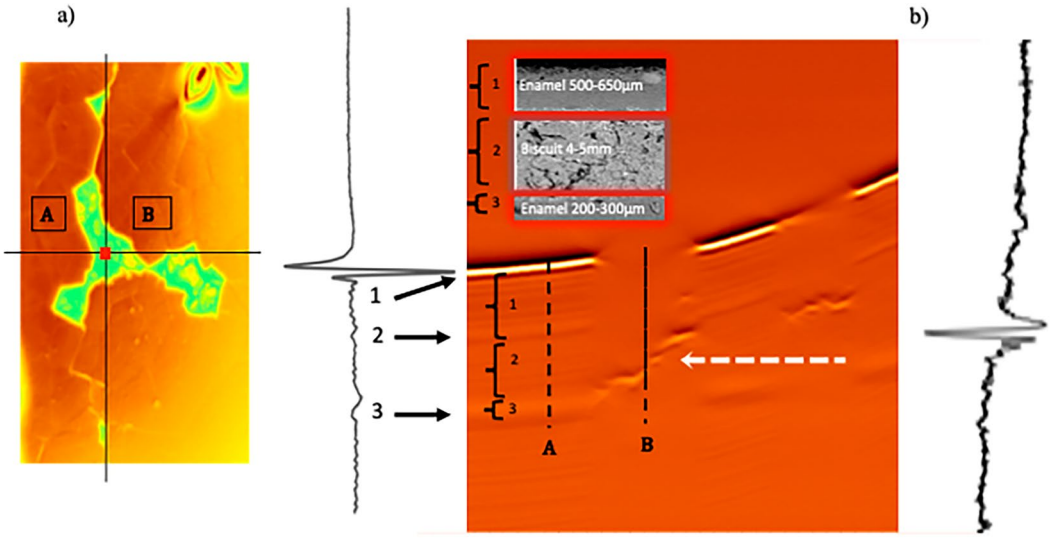

Figure 7. (**a**) C scan and (**b**) B -Scan through the main Fracture. The temporal position of the peaks delimits the biscuit and the enamel layers without ambiguity. Interface are numbered 1 : Air-glaze-interface, 2 Enamel-biscuit interface, 3 biscuit-back ceramic. , a schematic layer is in insert to describe the reflected time signal at the interfaces.

Endmembers	Colors	XRF results (Chromophores)	HSI Results (Chromophores & Spectral Characteristics)
1	Bright blue	Cu, Fe	Cu^{2+} (broad absorption 700–900 nm)
2	Turquoise green	Cu, Fe	Cu^{2+} (broad absorption 700–900 nm) Fe^{3+} (~ 440 nm)
3	Grey blue (bird wings)	Sn, Mn, Fe, Co, Zn	Co^{2+} (530 nm, 595 nm, 645 nm) Fe^{3+} (420 nm)
4	Light green	Cr, Fe, Cu	Cu^{2+} (broad absorption 700–900 nm) Cr^{3+}/Fe^{3+} (445 nm)
5	Green	Cr, Fe, Co, Cu, Zn	Cu^{2+} (broad absorption 700–900 nm) Cr^{3+}/Fe^{3+} (445 nm) Co^{2+} (595 nm, 645 nm)
6	Dark green	Cr, Mn, Fe, Co, Cu, Ni	Cu^{2+} (broad absorption 700–900 nm) Cr^{3+}/Fe^{3+}(445 nm)
7	Bright red	Cr, Fe	Inflection point at 650 nm
8	Violet_Bird neck	Cr, Fe, Sn (traces)	Fe^{3+} (420 nm and 440 nm) Inflection point at 650 nm
9	Red_bird chest	Ba, Cd, Fe, Co, Se	Inflection point 598 nm
10	Orange/red	Ba, Cd, Fe, Se	Inflection point 570 nm
11	Pink tree	Fe, Cu	SPR of Cu nanoparticles (555 nm)
12	Yellow	Cr, Fe	$PbCrO_4$ (inflection point at 515 nm
13	Gold leaf	Au, Ag, Pd, Zr, Fe	Inflection point at 600 nm
14	Black	Cr, Mn, Fe, Co, Cu, Zn	Cu^{2+} (broad absorption 700–900 nm) Cr^{3+}/Co^{2+} (648 nm)
15	Green label ink	Ba, Fe, Cr, Cu	Cu^{2+} (broad absorption 700–900 nm) Cr^{3+} (650 nm)
Behind the plate	Turquoise green	Fe, Cu	Cu^{2+} (broad absorption 700–900 nm)

Table 1. Elemental characterization by portable X-ray fluorescence (p-XRF), spectral characteristics, and the chromophores identified for each color implementing Hyperspectral Imaging Spectroscopy. Silicon (Si), lead (Pb), sulfur (S), potassium (K), and calcium (Ca) were identified in all areas, exhibiting the same proportions in the colored regions and the white area on the back of the plate.

Cobalt was identified as the chromophore in both the bird wings and the reflection in the water (endmember 3), with both areas appearing bright red in the IRFC image. The three characteristic absorption bands of Co^{2+} in tetrahedral coordination ($^4A_2(F) \rightarrow {}^4T_1(P)$) are visible around 530 nm, 595 nm, and 645 nm[29,30]. Additionally, one absorption peak of Fe^{3+} was observed at approximately 420 nm ($^6A_1 \rightarrow {}^4E(G)$)[3]. Furthermore, the elemental analysis revealed zinc, manganese, and antimony, most likely intentionally added to achieve the final greyish hue.

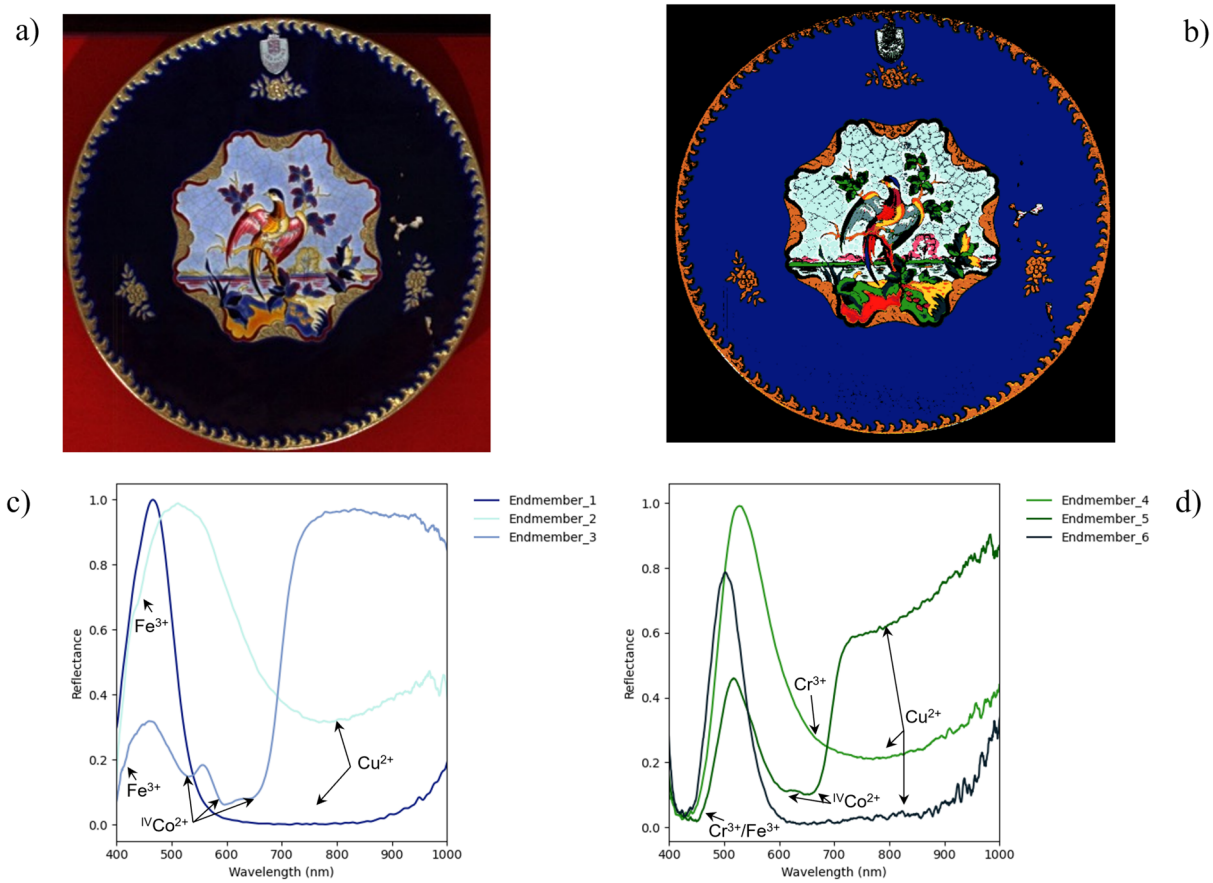

Figure 8. VNIR HSI results. (**a**) Infrared false colors (IRFC) image; (**b**) false color representation of the pigment distribution determined by SAM classification; Reflectance spectra (endmembers) of (**c**) blue and (**d**) green hues.

The leaves and vegetation scene incorporates three distinct green hues, from lighter to darker. These variations were achieved by introducing coloring agents, such as chromium, iron, and copper, with higher concentrations in the darker shades. A broad absorption around 800 nm is detectable in all three reflectance spectra attributed to Cu^{2+} ion absorption (Fig. 8d). Moreover, all spectra exhibit a peak around 445 nm, which may result from a shift in the first peak of Cr^{3+} (commonly found at 450 nm), possibly due to overlap with Fe^{3+} absorption. In the spectrum of light green (endmember 4), an absorption peak of Cr^{3+} at 690 nm is also slightly distinguishable[31]. The cobalt element is observable in the p-XRF of the two darker green hues, which is also well distinguishable in the absorbance spectrum of green leaves (endmember 5) by two absorbance peaks at 595 nm and 645 nm. Conversely, the absorbance is too high in the darkest hue (endmember 6), and the cobalt peaks are indistinguishable. In this latter hue, nickel and manganese have also been detected in noticeable amounts. The presence of Mn^{2+} ions might have contributed to the shift of the reflectance peak to a lower wavelength observed in endmember 6 (480 nm) compared to the other two spectra (520 nm and 540 nm, respectively in endmember 5 and 4), as manganese cations have an absorbance at around 430 nm[32]. The presence of manganese might be explained by its common use in the glass and ceramic industry, where pyrolusite (Mn_2O) is added to iron chromate ($Fe_2(CrO_4)_3$) to achieve dark colorations[33]. In contrast, the detected zinc in medium green leaves may have been added as network former. Zn^{2+} ions could influence cobalt in different manners: if present in high amounts, the ion increases the speciation of cobalt and reduces the distortion of the tetrahedral complex, providing, in turn, a bluish-green hue[34].

Concerning the other colors, various red shades were attained using chromium-based red pigments for bright reds and purples, while CdS_xSe_{1-x} nanocrystals were present in the red bird wings. Pink, on the other hand, was obtained using copper nanoparticles. Yellow was achieved using chromium-based pigments, potentially lead chromate. Black colors were obtained by mixing various oxides in high amounts (Cr, Mn, Fe, Co, Cu, and Zn). Finally, the investigation into gilding revealed a gold alloy, and the green ink used for ceramic production labels was found to be copper/chromium-based with traces of iron and barium. The comprehensive data from spectroscopic and elemental analyses of all these pigments is described in the "Annex".

In ceramic, the color is provided, at the level of the paste or the level of the enamel, by dyes, and pigments, specific to ceramic, which must resist the temperatures of ceramic firing. Most often, these are oxides or combinations of oxides.

Our experience shows that certain metal oxides are ceramic dyes, e.g. their powder is mixed with a paste or enamel provides color to the fired product. Here are some examples of the most common oxides and the colors

they give to an oxidized fired enamel: cobalt (blue), copper (green, blue), manganese (brown, purple), iron (yellowish, reddish, greenish), chrome (green, yellow, red), nickel (brown, greenish, gray), and there are others (uranium, titanium, vanadium, etc.). The intensity of the color increases with the level of coloring oxide which made the analysis very complex. The intensity of the color depends on the covering power of the oxide (for example cobalt oxide, 0.1% of this oxide will give a very powerful blue, while the same level of iron oxide will give a tint very pale). The achieved color by an oxide also depends on the characteristics of the product in (or on) which it is introduced. Let us look at iron oxide which will give yellowish tints in a paste rich in alumina and reddish tints when there is little alumina. While copper oxide gives blues in alkaline enamel and greens in lead enamel. Antimony oxide gives yellows (Naples yellow) in lead enamel and is practically not coloring in others. By mixing pure oxides, it is possible to obtain intermediate shades. When the quantity of oxide added to the enamel is too high, new shades can be obtained, for example, metallic shades, by saturation. The cooking temperature and atmosphere (reduction or oxidation) have an influence on the color given by an oxide. The color of the oxide mixed with the raw enamel (or paste) is often very different from the color after firing. These complex and unpredictable behaviors explain the need for meticulous testing but also the multitude of possibilities.

Moreover, pure or simply mixed coloring oxides do not make it possible to obtain all the desired shades of color. Manufacturers have developed very complete palettes of reliable colorings which often have similar shades before and after cooking. These dyes are obtained from coloring oxides and other compounds, purified, reduced to fine powder, measured, and mixed. These mixtures are calcined and sintered at high and precise temperatures. The mass obtained is crushed, washed with water, ground for a long time, and then dried. The composition of these dyes is often very complex and protected. Manufacturers offer palettes of dyes specific to different uses: mass dyes for clay products (paste and slip), enamel dyes, dyes for high temperatures (or large fire colors), and dyes for low temperatures (or small fire colors).

In this context, it seems almost out of reach to predict, classify, or compare the different reflectivity of these very complex materials even if chemometrics tools demonstrated some capabilities with binary or ternary mixtures[35]. Nevertheless, we observed clearly different reflectivity behavior correlated to some overlayer paintings such as the pink color on the trees, dark green on the leaves, and other colors on the Phoenix's throat and chest. An alternative analysis is under investigation to understand this clear different behavior due to chemical compounds or the presence of structural differences (nanoparticles) leading to a substantial modification of the dielectric response.

Conclusion

In this article, we used terahertz time-domain spectroscopy in reflection geometry as a tool for the earthenware art science. We were able to find hidden fractures that were initiated near a large one. On the large plate enamel colored sample, the bilayer structure of the ceramic and the substrate underneath the surface were presented. To perform this analysis, terahertz imaging with a Z-tracking system allowed for finding the real shape and dimensions of the plate. We could merge temporal information with good reflectivity while keeping the distance between the sample and the sensor constant over one centimeter in altitude. Such geometrical information was used to reconstruct in 3D the plate and could be extended to any non-flat object inspection. We demonstrated that terahertz spectroscopy and imaging can provide very useful information for the evaluation of the damage and conservation state of ceramic artwork or artist technique. Single point measurements by this technique can be used for a qualitative assessment of the internal structure of a piece, while imaging can be useful for careful measurement of the geometry and provides information about the artistic procedure. Finally, our terahertz imaging technique shows interesting results about the reflectivity of some colored pigments with clear differentiation. We performed an intensive and non-invasive analytical technique, X-ray fluorescence (p-XRF) and hyperspectral imaging spectroscopy (HSI), to characterize the glaze and the coloring agents in the decorative ceramic plate. Very complex compositions with many different elements were detected and provided an interesting understanding of the ceramic industrial palette. We can consider that terahertz spectroscopy and imaging will become useful tools in the field of art restoration and the earthenware community in the near future owing to their non-contact and non-destructive nature.

Data availability

The datasets used and/or analysed during the current study available from the corresponding author on reasonable request.

Annex

Let's remind you that the depth-of-field of the terahertz (THz) reflection is limited, as a result of the comparatively long (0.1 mm to a few mm) wavelength of the THz radiation used. In order to obtain the best potential lateral resolution, a short focal length must be used to focus the THz onto the target or sample. This results in a depth-of-field that is a few times the wavelength. Ideally, when imaging a planar object, we want to keep the target surface within a few hundred micrometers of the focal plane. With a nonplanar surface, it is impossible to maintain the surface at the focal plane over a large imaging area. For the Z-tracking, we have mounted a laser-range gauge at a 30-degree angle near the terahertz focusing optic with the THz head. Then the laser gauge provides a robust measurement of the distance to the target surface. Updates to the instrument embedded control software provide the control-loop to permit the head to track the target surface. In order to keep the terahertz focus at the object surface the instrument control system performs a raster scan with the laser range gauge some 10–20 scans before the terahertz focal spot as shown in Fig. 9. In order to track the target surface at the position of the THz focus, the instrument control system will perform a raster image scan with the raster orientation such that the laser gauge leads the THz focal point. Thus, the instrument can record the surface measured by the laser gauge ahead

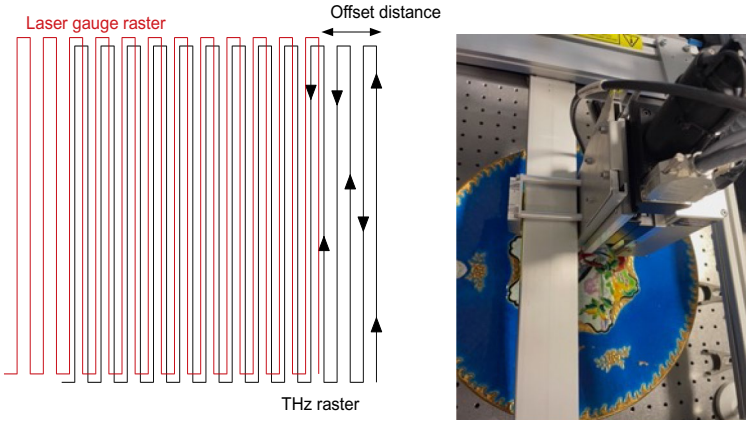

Figure 9. The offsets raster trajectories of the laser gauge target point relative to the THz focus are illustrated. Implementation into the setup.

of the THz position. The height of the Z-axis is updated continuously using the surface profile measured a few lines earlier in the measurement process. This keeps the terahertz beam focused on the surface of the object. The software allows the User to either keep the focus at the surface of the object or to offset the focus by up to 3 mm to examine the subsurface structure. We have verified the z-axis surface tracking control loop stability by stimulating the control system with a series of step-changes in the target position with a logarithmic increasing range of step sizes. The step sizes range from 100 µm up to 20 mm. The responsiveness of the control loop may be adjusted by a parameter set in the instrument configuration. For testing and demonstration purposes, we have used a small flattened aluminum scale to provide a non-planar test sample. The width is about 50 mm with different heights from 100 µm to 1 mm. We have used this to test the surface tracking algorithm.

In Fig. 10, B-scan reveals the time position of the metal interface. A Gaussian beam acquires a phase shift along the propagation direction; this phase shift differs from that of a plane wave propagating with the same optical frequency. This difference is known as the Gouy phase shift. That results in different images in frequency domain as shown in Fig. 10 and then artifacts. The result is a clear artifact since the metal interface is presenting different reflection coefficients varying with the time of flight out of the Rayleigh length, so a loss of intensity at different frequencies. With the tracker, only interfaces between two successive metallic levels are distinguishable in the B-scan since the distance between the focal silicon lens attached to the PCA and the target is kept constant, resulting in the same amplitude of the reflected THz beam on the different metal scale at the same frequency. Combining a perfect positioning of the sample and the time of flight obtained with the tracking gives a precise 3D rendering of the first interface, allowing the 3D shape of any samples.

Hyperspectral imaging (HSI) in visible and near-infrared (Vis–NIR) range

The visible near-infrared (Vis–NIR) hyperspectral camera, developed by SPECIM (Finland), was positioned vertically on a translation rail controlled by the Spectral IDAQ software. The rail, affixed to two tripods, measured 1.30 m and enabled the horizontal movement of the camera system. The two halogen lamps were positioned at a 45° angle from the sample, moving along the translation rail simultaneously with the camera. This synchronized

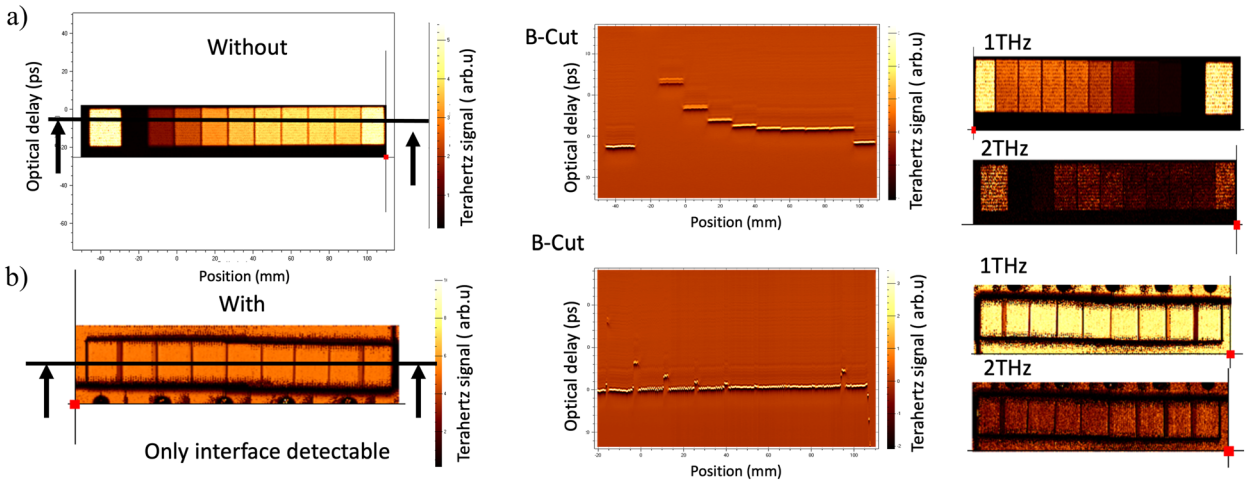

Figure 10. Demonstration of Z tracker: (**a**) Peak-to-peak images, B-scan and Amplitude of the FFT at 1 and 2 THz without tracking, (**b**) with tracking option.

movement guaranteed consistent illumination throughout the entire scanning process. The hyperspectral system has an HS-XX-V10E CCD detector with a spectral resolution (FWHM) of 2.8 nm, a spectral sampling of 0.7 nm, and a pixel size of 54.7 μm^2. The moving camera allows for the building of a data cube where the first two dimensions are spatial (1600 pixels × X pixels) (with X corresponding to the number of pixels in the width of the image). The third dimension is a spectral dimension (840 bands). The wavelength range extends between 400 and 1000 nm. The focal length is 23 mm. For the study, the experimental conditions were a working distance of 84 cm, scan speed of 13 mm/s, and an exposure time of 25 ms. Spectral IDAQ software provided spectra acquisition, storage, and calibration. Before each session, both white and dark field calibrations were conducted. A Spectralon fluoropolymer (99% reflectance) was used as white reference to calibrate the reflectance spectra. A following acquisition with the shutter closed was performed and used as a dark reference to quantify the detector's electronic noise. The ceramic plate was illuminated with two halogen lamps oriented at 45° from the sample.

Data treatment

The data cube was treated with ENVI 5.2 +IDL software (Harris Geospatial). False color images were generated by substituting an infrared band for the red channel and selecting two other bands in the visible range for the green and blue channels (R → 900 nm; G → 650 nm; B → 550 nm) in the ENVI software. The IRFC (Infrared False color) images helped distinguish chromogen agents of similar color but different compositions. ENVI's Spectral Hourglass Wizard (ENVI-SHW) was implemented to identify, extract, and map the reference spectra. The processing flow implemented the Minimum Noise Fraction (MNF) technique to reduce noise and enhance data quality, followed by the isolation of 'spectrally pure' pixels through the Pixel Purity Index (PPI) using 10,000 reflectance spectra with a threshold of 2.5. The n-D Visualizer (a 3D scatter plot) was employed to manually identify the clusters defining the dataset's purest pixels (endmembers). Once the endmembers were extracted, the SAM mapping method visualized their distribution in the image. This algorithm calculates, for each pixel (in radians), the angle between the image's reflectance spectrum and the chosen endmember. The histogram threshold was manually adjusted for each case to ensure a close match between the spectral characteristics of the identified spatial pixels and the target endmember. The tolerance range of the study varied for the hyperspectral cube, ranging from 0.17 to 0.4 radians. Only endmembers representative of the chromophores were selected and investigated. The spectra of the endmembers have all been presented as Reflectance.

Handheld XRF analysis

The elemental analysis was performed using the portable Olympus Vanta VCR-CCX-G2 analyzer. The detector is large 13 mm^2 silicon SDD with < 140 eV FWHM resolution at Kα of Mn. The spot is 10 mm or 3 mm in diameter with an integrated camera (variable collimator). Two beams (40 kV and 10 kV) are automatically sequenced, and the total analysis time is 30 s. Data treatment was performed using PyMCA software.

Results from spectroscopic and elemental analyses

Hyperspectral imaging spectroscopy (HSI) and p-XRF were jointly employed to identify the coloring agents. The elemental composition of the glaze was ascertained through portable X-ray fluorescence spectroscopy (p-XRF). Silicon (Si), lead (Pb), sulfur (S), potassium (K), and calcium (Ca) were identified in all areas, exhibiting the same proportions in the colored regions and the white area on the back of the plate.

From hyperspectral analysis, we have identified and localized 15 main endmembers that characterize the pigments used in Longwy plate coloration. Figure 11 depicts the ensemble of these spectra and their representation through a false-color image obtained by SAM classification. The characterization of these endmembers was then sorted by color; detailed descriptions of blues and greens are provided in section "Discussion" of the

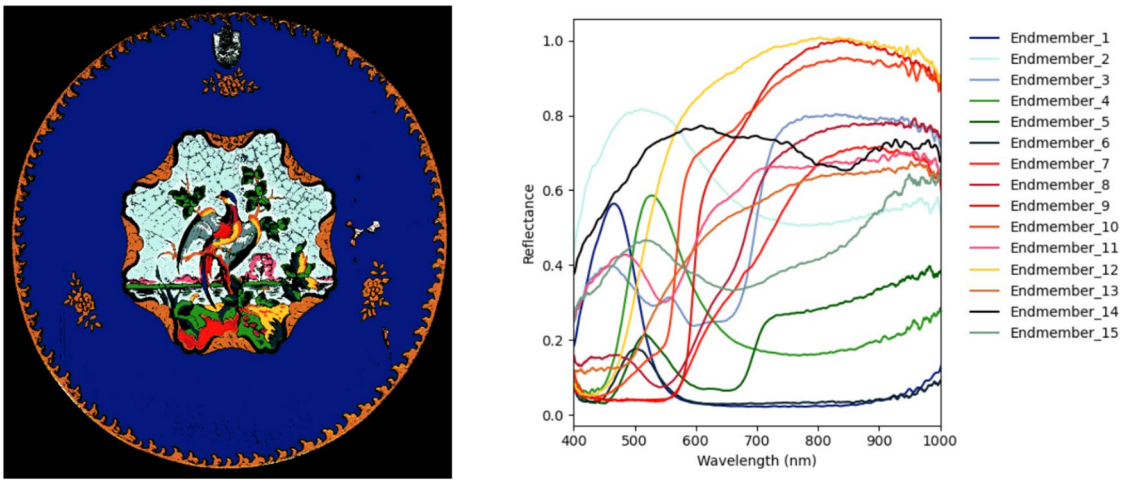

Figure 11. False color representation of the pigment distribution determined by SAM classification (left) and reflectance spectra of the extracted endmembers (right).

article, while the remaining colors (red, pink, yellow, gold leaf, black pigments, and the green ink used in the label) are presented and discussed here.

Red and pink colors

The bright red (endmember 7) and the more violet color of the bird's neck (endmember 8) were attributed to pigments based on chromium and iron. The two absorbance spectra exhibit an inflection point at 650 nm; the violet also shows two absorbance peaks attributable to Fe^{3+} (420 nm and 440 nm). The definitive identification of the chromium-doped red pigment is challenging. The absence of elements like Sn or Zn rules out the possibility of Cr-doped malayaite ($CaSnSiO_5$) or Cr-doped gahnite (Cr: $ZnAl_2O_4$)[17]. The lead content appeared with the same intensity as the other colors investigated, suggesting the exclusion of lead chromite. Possible alternatives include a synthesized spinel (Cr^{3+}: $MgAl_2O_4$) or $Al_{(2-x)}Cr_xO_3$-based pigments. Spinels were first synthesized at the Manufacture de Sèvres by Ebelmen around the middle of the nineteenth century[36]. Further analyses, such as XRD, are required.

Two additional hues of red have been identified in the scene as depicted in Fig. 12, one utilized for the bird's chest (endmember 9) and the other for painting the upper part of the wings (endmember 10). The hypothesis of coloration through the precipitation of mixed $CdS_xSe_{(1-x)}$ nanocrystals has been formulated based on p-XRF results, as both cadmium and selenium were detected in these two areas. The reflectance spectra further support the assumption of semiconductor nanoparticles. According to the literature, the inflection point of the curve shows a shift towards higher wavelengths when changing the chemical composition from CdS (yellow colors) toward CdSe (red colors), passing through different CdS-CdSe solid solutions (orange colors)[37]. The inflection points of the two investigated regions were at 570 nm for the more orange color (endmember 10) and at 598 nm for the more reddish one (endmember 9), showing good consistency with previous research[38].

The elemental analysis also provided the observation of other elements, including barium, iron and, in the darker hue, traces of cobalt.

The elemental analysis of the pink hue observed in the trees and bushes revealed the presence of iron and copper. The integration with the spectroscopic data strongly suggested the implementation of copper nanoparticles (Cu^0) whose surface plasmonic resonance (SPR) is approximately 555 nm[39]. Commonly, variations in positions and shapes observed in the SPR band are related to the changes in size and dimension of the copper nanoparticles.

Yellow color and gold leaf

Elemental analysis showed in Fig. 13 the presence of chromium and iron in the yellow color. The absorbance peak at 425 nm and an inflection point at 515 nm observed in the reflectance spectrum (endmember 12) might suggest the use of yellow chrome pigment ($PbCrO_4$)[40]. However, further investigations are required to confirm this hypothesis. The elemental composition of the gold leaf resulted in a gold alloy comprised of gold, traces of silver, palladium, zirconium, and iron. The reflectance spectrum presented an absorbance at around 520 nm and an inflection point at 590 nm.

Black color

Based on experimental data and existing literature, it was assumed that the black pigment was produced through the calcination of various oxides, resulting in the formation of the spinel structure composed of di- and trivalent cations[41]. The elemental composition analysis of Fig. 14 revealed the presence of chromium, manganese, iron, cobalt, copper, and zinc. The reflectance spectra also detected different absorbance peaks corresponding to the present cations. For instance, the broad absorbance at 800 nm was attributed to Cu^{2+}, while the absorption band around 648 nm suggested the contribution of Co^{2+} and Cr^{3+} absorption.

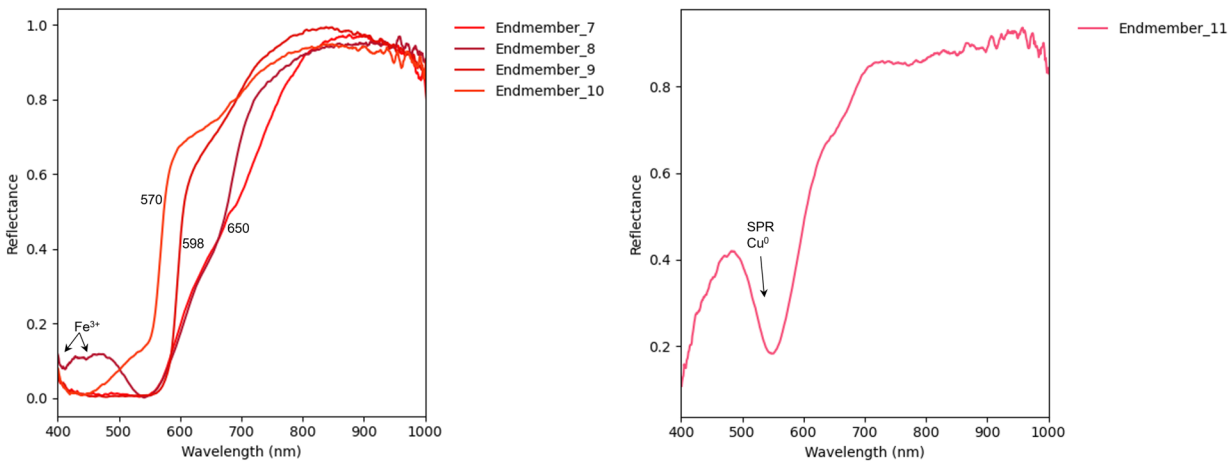

Figure 12. Reflectance spectra of red (left) and pink (right) hues.

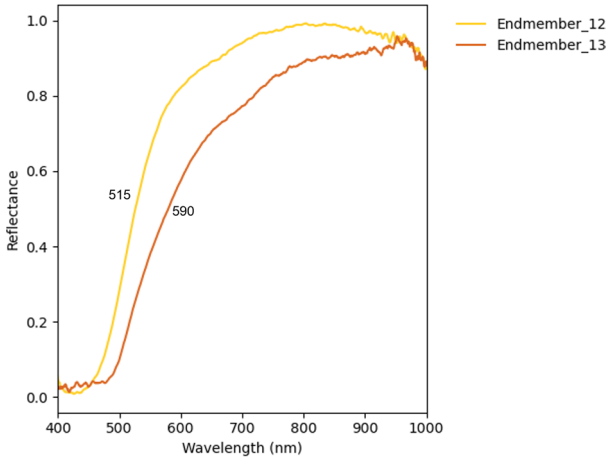

Figure 13. Reflectance spectra of yellow and gold leaf.

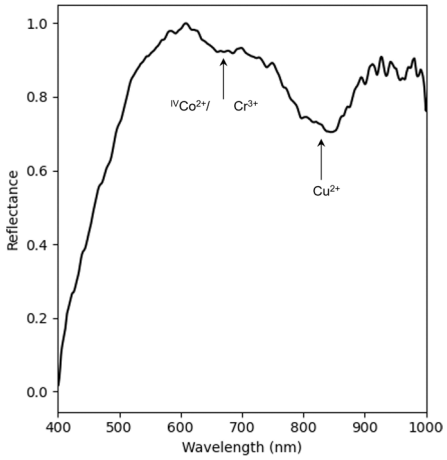

Figure 14. Reflectance spectrum of black hue.

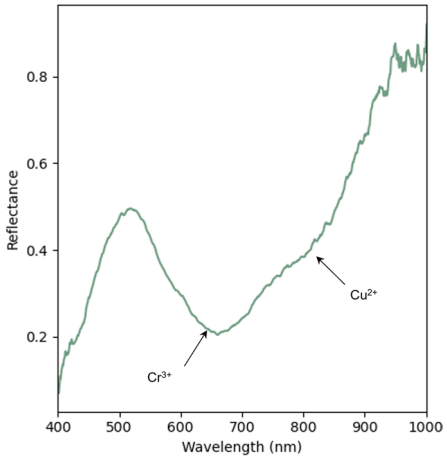

Figure 15. Reflectance spectrum of the green ink used for the ceramic production label.

Green ink used for the ceramic production label
Attached to the plate there is the original label from the plate's manufacturing company, Longwy. Analyses of the green ink used in this label revealed the presence of copper, chromium, barium, and iron. HSI absorbance spectra exhibit a broad band at 660 nm, characteristic of Cr^{3+} absorption ($^4A_{2g}$—> $^4T_2$)[6]. In Fig. 15, Cu^{2+} ions were identified by a slight absorbance peak between 800 and 900 nm.

Terahertz time-domain spectroscopy

The samples were measured with a fiber-coupled, commercial Terapulse Lx THz-TDS spectrometer manufactured by TeraView LTD. The setup was arranged in a reflection configuration. An 18 mm focal length silicon lens collimates the THz radiation from the emitter and focuses it onto the sample. Likewise, the THz radiation is reflected through the sample, and an 18 mm focal length silicon lens focuses it into the receiver. For each sample, ten measurements at random positions on the sample were recorded followed by a single reference measurement where the sample was absent. All the measurements were performed under the same ambient experimental conditions recording time traces with a length of 50 ps and 1000 acquisitions (scan speed: 60 traces/s). Before calculating the reflection function in the frequency domain as described in equation (1), the obtained time-domain signals were artificially extended to 60 ps by zero-padding to ensure that the measured pulse was positioned before the midpoint of the time window.

Received: 10 April 2024; Accepted: 6 August 2024
Published online: 20 August 2024

References

1. Cosentino, A. Terahertz and cultural heritage science: Examination of art and archaeology. *Technol. (Basel)* **4**(1), 6. https://doi.org/10.3390/technologies4010006 (2016).
2. Fukunaga, K. Nondestructive evaluation of lined paintings by THz pulsed time-domain imaging. *Heritage* **6**(4), 3448–3460. https://doi.org/10.3390/heritage6040183 (2023).
3. Krügener, K. *et al.* Terahertz meets sculptural and architectural art: Evaluation and conservation of stone objects with T-ray technology. *Sci. Rep.* **5**, 14842. https://doi.org/10.1038/srep14842 (2015).
4. Fukunaga, K., Ogawa, Y., Hayashi, S. & Hosako, I. Terahertz spectroscopy for art conservation. *IEICE Electron. Express* **4**(8), 258–263 (2007).
5. Koch-Dandolo, C. L., Filtenborg, T., Fukunaga, K., Skou-Hansen, J. & Jepsen, P. U. Reflection terahertz time-domain imaging for analysis of an 18th century neoclassical easel painting. *Appl. Opt.* **54**(16), 5123. https://doi.org/10.1364/AO.54.005123 (2015).
6. Abraham, E., Younus, A., Delagnes, J.-C.C.J.C. & Mounaix, P. Non-invasive investigation of art paintings by terahertz imaging. *Appl. Phys. A Mater. Sci. Process.* **100**(3), 585–590. https://doi.org/10.1007/s00339-010-5642-z (2010).
7. Zhong, H. *et al.* Nondestructive defect identification with terahertz time-of-flight tomography. *IEEE Sens. J.* **5**(2), 203–208. https://doi.org/10.1109/jsen.2004.841341 (2005).
8. Cassar, Q. *et al.* Characterization of Varnish ageing and its consequences on terahertz imagery: Demonstration on a painting presumed of the French renaissance. *J. Infrared Millim Terahertz Waves* **41**(12), 1556–1566. https://doi.org/10.1007/s10762-020-00733-y (2020).
9. Dong, J., Locquet, A., Melis, M. & Citrin, D. S. Global mapping of stratigraphy of an old-master painting using sparsity-based terahertz reflectometry. *Sci. Rep.* **7**(1), 1–12. https://doi.org/10.1038/s41598-017-15069-2 (2017).
10. Koch-Dandolo, C., Cosentino, A. & Jepsen, P. U. Inspection of panel paintings beneath gilded finishes using terahertz time-domain imaging. *Stud. Conserv.* **60**(1), S159–S166. https://doi.org/10.1179/0039363015Z.000000000220 (2015).
11. Picollo, M., Fukunaga, K. & Labaune, J. Obtaining noninvasive stratigraphic details of panel paintings using terahertz time domain spectroscopy imaging system. *J. Cult. Herit.* **16**(1), 73. https://doi.org/10.1016/j.culher.2014.01.006 (2015).
12. Mikerov, M., Shrestha, R., van Dommelen, P., Mittleman, D. M. & Koch, M. Analysis of ancient ceramics using terahertz imaging and photogrammetry. *Opt. Express* **28**(15), 22255. https://doi.org/10.1364/oe.399336 (2020).
13. Niijima, S., Taniguchi, H., Murate, K. & Kawase, K. Terahertz spectroscopy applied to estimation of firing temperatures of ancient ceramics. *IEEE Trans. Terahertz Sci. Technol.* **12**(3), 300–306. https://doi.org/10.1109/TTHZ.2022.3153554 (2022).
14. Manca, R. *et al.* Non-invasive characterization of maiolica layer structure by terahertz time-domain imaging. *Coatings* **13**, 7. https://doi.org/10.3390/coatings13071268 (2023).
15. Catapano, I., Affinito, A., Guerriero, L., Bisceglia, B. & Soldovieri, F. Majolica imaging with THz waves: Preliminary results. *Appl. Phys. A Mater. Sci. Process* **122**(5), 1–11. https://doi.org/10.1007/s00339-016-0055-2 (2016).
16. Finlay, R., Journal, S. & Fall, N. The pilgrim art: The culture of porcelain in world history the pilgrim art: The culture of porcelain in world history. In *i619 Philip III of Spain Made a Ceremonial Entrance into Lisbon, vol. 9*, 141–187 (2016).
17. Beauvoit, E., Ben-Amara, A., Chapoulie, R. & Lemasson, Q. A multianalytical approach for the study of relief polychrome glazed ceramics (France, 19th century). *J. Archaeol. Sci. Rep.* **51**, 104176. https://doi.org/10.1016/j.jasrep.2023.104176 (2023).
18. Kleist, E. M. & Korter, T. M. Quantitative analysis of minium and vermilion mixtures using low-frequency vibrational spectroscopy. *Anal. Chem.* **92**(1), 1211–1218. https://doi.org/10.1021/acs.analchem.9b04348 (2020).
19. Kleist, E., Dandolo, C. L. K., Guillet, J.-P.J.-P., Mounaix, P. & Korter, T. M. Terahertz spectroscopy and quantum mechanical simulations of crystalline copper-containing historical pigments. *J. Phys. Chem. A* **123**(6), 1225–1232. https://doi.org/10.1021/acs.jpca.8b11676 (2019).
20. Recur, B. *et al.* Ordered subsets convex algorithm for 3D terahertz transmission tomography. *Opt. Express* **22**(19), 23299. https://doi.org/10.1364/OE.22.023299 (2014).
21. Cassar, Q. *et al.* Iterative tree algorithm to evaluate terahertz signal contribution of specific optical paths within multi-layered materials. *IEEE Trans. Terahertz Sci. Technol.* **9**(6), 684–694. https://doi.org/10.1109/tthz.2019.2937208 (2019).
22. Withayachumnankul, W. & Naftaly, M. Fundamentals of measurement in terahertz time-domain spectroscopy. *J. Infrared Millim. Terahertz Waves* **35**(8), 610–637 (2014).
23. Zhang, Y. *et al.* Extracting complex refractive index from polycrystalline glucose with self-referenced method for terahertz time-domain reflection spectroscopy. *Appl. Spectrosc.* **70**(7), 1102–1108 (2016).
24. Cassar, Q. *et al.* Terahertz refractive index—based morphological dilation for breast carcinoma delineation. *Sci. Rep.* **1–16**, 2021. https://doi.org/10.1038/s41598-021-85853-8 (2021).
25. Pastorelli, G. *et al.* Characterisation of historic plastics using terahertz time-domain spectroscopy and pulsed imaging. *Anal. Bioanal. Chem.* **403**(5), 1405–1414. https://doi.org/10.1007/s00216-012-5931-9 (2012).

26. Sciuto, C. *et al.* What lies beyond sight? Applications of ultraportable hyperspectral imaging (VIS-NIR) for archaeological fieldwork. *J. Field Archaeol.* **47**(8), 522–535. https://doi.org/10.1080/00934690.2022.2135066 (2022).
27. Cherian, C. *et al.* Preliminary non-invasive study of Roman glasses from Jesolo (Venice), Italy. *Glass Technol. Eur. J. Glass Sci. Technol. Part A* **61**(1), 1–15. https://doi.org/10.13036/17533546.61.1.003 (2020).
28. Palomar, T. *et al.* Analysis of chromophores in stained-glass windows using Visible Hyperspectral Imaging in-situ. *Spectrochim. Acta A Mol. Biomol. Spectrosc.* **223**, 117378. https://doi.org/10.1016/j.saa.2019.117378 (2019).
29. Aceto, M. *et al.* A fast non-invasive method for preliminary authentication of mediaeval glass enamels using UV–visible–NIR diffuse reflectance spectrophotometry. *J. Cult. Herit.* **45**, 33–40. https://doi.org/10.1016/j.culher.2020.05.003 (2020).
30. Bacci, M. & Picollo, M. Non-destructive spectroscopic detection of cobalt(II) in paintings and glass. *Stud. Conserv.* **41**(3), 136–144. https://doi.org/10.1179/sic.1996.41.3.136 (1996).
31. Meulebroeck, W., Wouters, H., Nys, K. & Thienpont, H. Authenticity screening of stained glass windows using optical spectroscopy. *Sci. Rep.* **6**(1), 37726. https://doi.org/10.1038/srep37726 (2016).
32. Paul, A. Coloured glasses. In *Chemistry of Glasses* (ed. Paul, A.) 204–276 (Springer, 1982). https://doi.org/10.1007/978-94-009-5918-7_7.
33. Weyl, W. A. *Coloured Glasses* (Dawson's of Pall Mall, 1959). https://books.google.it/books?id=TuRevgAACAAJ.
34. Ahmad, F., Hassan-Aly, E., Atef, M. & ElOkr, M. M. Study the influence of zinc oxide addition on cobalt doped alkaline earth borate glasses. *J. Alloys Compd.* **593**, 250–255. https://doi.org/10.1016/j.jallcom.2014.01.067 (2014).
35. Sleiman, J. B., Bousquet, B., Palka, N. & Mounaix, P. Quantitative analysis of hexahydro-1,3,5-trinitro-1,3,5, triazine/pentaerythritol tetranitrate (RDX-PETN) mixtures by terahertz time domain spectroscopy. *Appl. Spectrosc.* **69**(12), 1464–1471. https://doi.org/10.1366/15-07937 (2015).
36. Verger, L. *et al.* Synthesis, properties and uses of chromium-based pigments from the Manufacture de Sèvres. *J. Cult. Herit.* **30**, 26–33. https://doi.org/10.1016/j.culher.2017.09.012 (2018).
37. Bach, H. & Neuroth, N. *The Properties of Optical Glass* (Springer Science & Business Media, 1998). https://books.google.it/books?id=J0RX1mbhzAEC.
38. Fornacelli, C., Colomban, P. & Turbanti-Memmi, I. Toward a Raman/FORS discrimination between Art Nouveau and contemporary stained glasses from CdSxSe1−x nanoparticles signatures. *J. Raman Spectrosc.* **46**(11), 1129–1139. https://doi.org/10.1002/jrs.4758 (2015).
39. Babini, A., Green, P., George, S. & Hardeberg, J. Y. Comparison of hyperspectral imaging and fiber-optic reflectance spectroscopy for reflectance and transmittance measurements of colored glass. *Heritage* **5**(3), 1401–1419. https://doi.org/10.3390/heritage5030073 (2022).
40. Otero, V., Carlyle, L., Vilarigues, M. & Melo, M. J. Chrome yellow in nineteenth century art: Historic reconstructions of an artists' pigment. *RSC Adv.* **2**(5), 1798–1805. https://doi.org/10.1039/C1RA00614B (2012).
41. Colomban, P., Sagon, G. & Faurel, X. Differentiation of antique ceramics from the Raman spectra of their coloured glazes and paintings. *J. Raman Spectrosc.* **32**(5), 351–360. https://doi.org/10.1002/jrs.704 (2001).

Acknowledgements

This research benefited from the scientific framework of the University of Bordeaux's IdEx "Investments for the Future" program/ GPR "Human Past".

Author contributions

P.M. designed the experiments and wrote the manuscript; FF. performed the experiments, PM, RC, FG,FF, PFT, AM, A BA, and GM made spectroscopic data analysis, and wrote the section of the manuscript on the data analysis. All authors contributed to writing the manuscript; PM. supervised all aspects of the project.

Competing interests

The authors declare no competing interests.

Additional information

Supplementary Information The online version contains supplementary material available at https://doi.org/10.1038/s41598-024-69697-6.

Correspondence and requests for materials should be addressed to P.M.